ADVANCED MATERIALS
www.advmat.de

Designing Mechanical Metamaterials with Kirigami-Inspired, Hierarchical Constructions for Giant Positive and Negative Thermal Expansion

Xiaogang Guo, Xiaoyue Ni, Jiahong Li, Hang Zhang, Fan Zhang, Huabin Yu, Jun Wu, Yun Bai, Hongshuai Lei, Yonggang Huang, John A. Rogers, and Yihui Zhang**

Advanced mechanical metamaterials with unusual thermal expansion properties represent an area of growing interest, due to their promising potential for use in a broad range of areas. In spite of previous work on metamaterials with large or ultralow coefficient of thermal expansion (CTE), achieving a broad range of CTE values with access to large thermally induced dimensional changes in structures with high filling ratios remains a key challenge. Here, design concepts and fabrication strategies for a kirigami-inspired class of 2D hierarchical metamaterials that can effectively convert the thermal mismatch between two closely packed constituent materials into giant levels of biaxial/uniaxial thermal expansion/shrinkage are presented. At large filling ratios (>50%), these systems offer not only unprecedented negative and positive biaxial CTE (i.e., −5950 and 10 710 ppm K^{-1}), but also large biaxial thermal expansion properties (e.g., > 21% for 20 K temperature increase). Theoretical modeling of thermal deformations provides a clear understanding of the microstructure–property relationships and serves as a basis for design choices for desired CTE values. An Ashby plot of the CTE versus density serves as a quantitative comparison of the hierarchical metamaterials presented here to previously reported systems, indicating the capability for substantially enlarging the accessible range of CTE.

Most natural materials expand isotropically upon heating because the kinetic energy of molecules increases their range of motion in non-parabolic atomic potentials, thereby offering positive thermal expansion coefficients (CTEs), most of which are in the range from ≈1 to 300 ppm K^{-1}. Recent studies demonstrate that mechanical metamaterials with optimized microstructure architectures can yield unconventional thermal expansion behaviors, such as near-zero thermal expansion,[1–5] negative thermal expansion,[6–11] and thermally induced shear.[12] These mechanical metamaterials are of increasing interest, because of their potential for use in applications such as high-precision space optical systems,[13,14] adaptive connecting components in satellites,[15,16] flexible MEMS that require excellent thermal stability,[17–24] battery electrodes with

Dr. X. Guo, H. Zhang, Dr. F. Zhang, J. Wu, Prof. Y. Zhang
AML
Department of Engineering Mechanics
Center for Flexible Electronics Technology
Tsinghua University
Beijing 100084, China
E-mail: yihuizhang@tsinghua.edu.cn

Dr. X. Guo, H. Yu, Dr. H. Lei
Institute of Advanced Structure Technology
Beijing Institute of Technology
Beijing 100081, China

Dr. X. Ni, Prof. J. A. Rogers
Center for Bio-Integrated Electronics
Northwestern University
Evanston, IL 60208, USA
E-mail: jrogers@northwestern.edu

J. Li, Y. Bai, Prof. Y. Huang, Prof. J. A. Rogers
Department of Materials Science and Engineering
Northwestern University
Evanston, IL 60208, USA

Prof. Y. Huang, Prof. J. A. Rogers
Department of Mechanical Engineering
Northwestern University
Evanston, IL 60208, USA

Prof. Y. Huang
Department of Civil and Environmental Engineering
Northwestern University
Evanston, IL 60208, USA

Prof. J. A. Rogers
Simpson Querrey Institute
Northwestern University
Chicago, IL 60611, USA

Prof. J. A. Rogers
Department of Biomedical Engineering
Northwestern University
Evanston, IL 60208, USA

Prof. J. A. Rogers
Department of Chemistry
Northwestern University
Evanston, IL 60208, USA

Prof. J. A. Rogers
Department of Electrical and Computer Engineering
Northwestern University
Evanston, IL 60208, USA

Prof. J. A. Rogers
Department of Neurological Surgery
Northwestern University
Evanston, IL 60208, USA

The ORCID identification number(s) for the author(s) of this article can be found under https://doi.org/10.1002/adma.202004919.

DOI: 10.1002/adma.202004919

unique thermal expansion,[25–29] dental fillings,[30] thermally controlled shape-changing structures,[12,31–48] etc. In response to these opportunities, diverse metamaterial designs have been reported, either for the purpose of maintaining the original shape during temperature changes, or for matching the thermal expansion properties of surrounding/supporting components. For example, advanced framework materials (e.g., metallic glasses,[49] ceramics,[50] crystals[51–53]) driven by phonons or electronic transitions were shown to exhibit negative CTE by exploiting optimal atomic lattice configurations. These materials, however, have a limited level of design freedom due to the difficulty in tailoring the atomic constructions, and they also suffer from the inherent brittleness, which limits their practical applications. In comparison, mechanical metamaterials that consist of microscale or larger structural building blocks offer substantially enhanced design freedom, owing in part to the fast development of additive manufacturing and micro-fabrication techniques in recent years. These systems usually exploit two engineering materials with different CTEs laminated into filaments and then structured into specific, periodic, cellular configurations to render tailorable negative/positive CTEs and anisotropic thermal expansion responses. Various microstructure configurations, such as triangular/hexagonal lattices,[8,54–63] chiral lattices,[6,7] auxetic structure designs,[64–66] and others,[67,68] have been systematically studied to reveal the structure–property relationships. The underlying mechanisms mainly involve the conversion of local deflections induced by thermal mismatch into unusual, effective, thermal responses of the mechanical metamaterials. Although each example offers specific features and capabilities for achieving unconventional effective CTEs, none is without limitations, either in terms of a limited range of tailorable CTE, a narrow temperature window to render unusual thermal responses, or a restricted degree of effective thermal deformations. In particular, the design and fabrication of mechanical metamaterials that combine a broad-range tunability of CTE (e.g., ≈ −2000 to 2000 ppm K^{-1}) and a capability for large thermal deformations (e.g., >10%) remain as key challenges. Additionally, the aforementioned mechanical metamaterials mostly exhibit relative low filling ratios (e.g., <50%), posing engineering constraints on their operation in devices that require large effective filling ratios.

Inspired by the concepts of kirigami and origami,[31,69–71] the ancient arts of paper cutting and folding, this paper introduces a highly filled, hierarchical metamaterial design capable of offering a broad range of tunability in CTE as well as large thermal deformations. These 2D hierarchical designs exploit closely packed arrangements of two different engineering materials, and magnify the thermal mismatch to achieve giant effective thermal expansion/shrinkage. In particular, the layouts allow for not only a large filling ratio (>50%), a large biaxial thermal expansion (>21% for 20 K temperature increase), but also a tunability in the biaxial CTE from −5950 to 10 710 ppm K^{-1}. The performance is even higher for uniaxial thermal responses, reaching >45% thermal strain, and a CTE tunability of ≈ −11 550 to 26 110 ppm K^{-1}. Comparison of these CTE characteristics to those of past metamaterial designs in the form of an Ashby plot clearly shows the capabilities of concepts reported here for enlarging substantially the accessible CTE range. Combined theoretical and experimental studies show that these mechanical metamaterials exhibit linear responses in thermal strain with respect to changes in temperature, in a range of practical interest.

Figure 1a illustrates schematically the hierarchical construction of kirigami-inspired metamaterial designs capable of isotropic thermal expansion. The structure follows from a linear array of the periodic unit element shown in the middle panel. The unit consists of a square base (length L_1) in the center and four identical structural branches (length L_2) with kirigami patterns. The branches serve as actuating components that convert bending deformations of bilayer beams into large uniaxial thermal expansion, while the central base, as a passive support, connects the actuating components to form a square lattice pattern. In the examples described here, the bilayer beam is composed of PI (in yellow, Young's modulus E_{PI} = 3 GPa, and CTE α_{PI} = 30 ppm K^{-1}) and poly(methyl methacrylate) (PMMA) (in red, Young's modulus E_{PMMA} = 3 GPa, and CTE α_{PMMA} = 70 ppm K^{-1}). As shown in the right of Figure 1a, the fundamental actuating element can be characterized by five key non-dimensional geometric parameters, including W_{PMMA}/W_{PI}, W_{Gap}/W_{PI}, L_{PI}/W_{PI}, L_{PMMA}/L_{PI}, and L_{Joint}/L_{PI}, where L_{PI} and L_{PMMA} are the lengths of PI and PMMA; W_{PI} and W_{PMMA} are the widths of PI and PMMA; L_{Joint} and W_{Gap} are the length of central joint and the gap between the neighboring bilayer beams, respectively. The total vertical length (L_e) of the fundamental actuating element can be then given by $L_e = 2L_{PI} + L_{Joint}$. Due to the difference ($\Delta\alpha = \alpha_{PMMA} - \alpha_{PI}$) in the CTE of PI and PMMA, the mismatch of thermal strain in these two materials leads to bending deflections of the bilayer beam, thereby yielding a large thermal expansion of the fundamental actuating element along the x-direction. As a result, the entire kirigami-inspired mechanical metamaterial, as shown in the left of Figure 1a, is capable of large biaxial thermal expansion. Figure 1b presents optical images of a representative specimen captured before (marked by the blue dashed line) and after heating (marked by the red solid line), with a temperature change from 26 to 56 °C by placing the material in a water bath, along with the deformed configuration predicted by finite element analyses (FEA; see Experimental Section for details). Here, the geometric parameters are W_{PMMA}/W_{PI} = 1, W_{Gap}/W_{PI} = 1, L_{PI}/W_{PI} = 62.8, L_{PMMA}/L_{PI} = 0.8, L_{Joint}/W_{PI} = 20, L_e/L_1 = 0.86, L_2/L_1 = 0.35, and W_{PI} = 100 µm. The fabrication method involves drop-casting, laser cutting, and wet etching technologies in sequence (see Experimental Section and Figure S1, Supporting Information, for details), to enable precise patterning of the specimen with feature sizes down to ≈100 µm. The thermal strain $\varepsilon_{meta,h}$, defined by the relative length change ($\Delta L/(L_1 + 2L_2)$) of the representative unit cell, reaches ≈16.8% for a 30 °C temperature increase in experiment, which agrees well with FEA prediction (≈15.8%). The observed deformations also show excellent agreement with FEA calculations (Figure S2, Supporting Information). These results demonstrate capabilities for achieving giant effective CTE (e.g., >5600 ppm K^{-1}) along both x and y-directions. Note that the passive central base in the metamaterial design is not necessary if the focus is on realizing a giant uniaxial CTE. Such a simplification of the design allows for an even larger thermal expansion, as shown in Figure S2, Supporting Information. As an example, the design with the

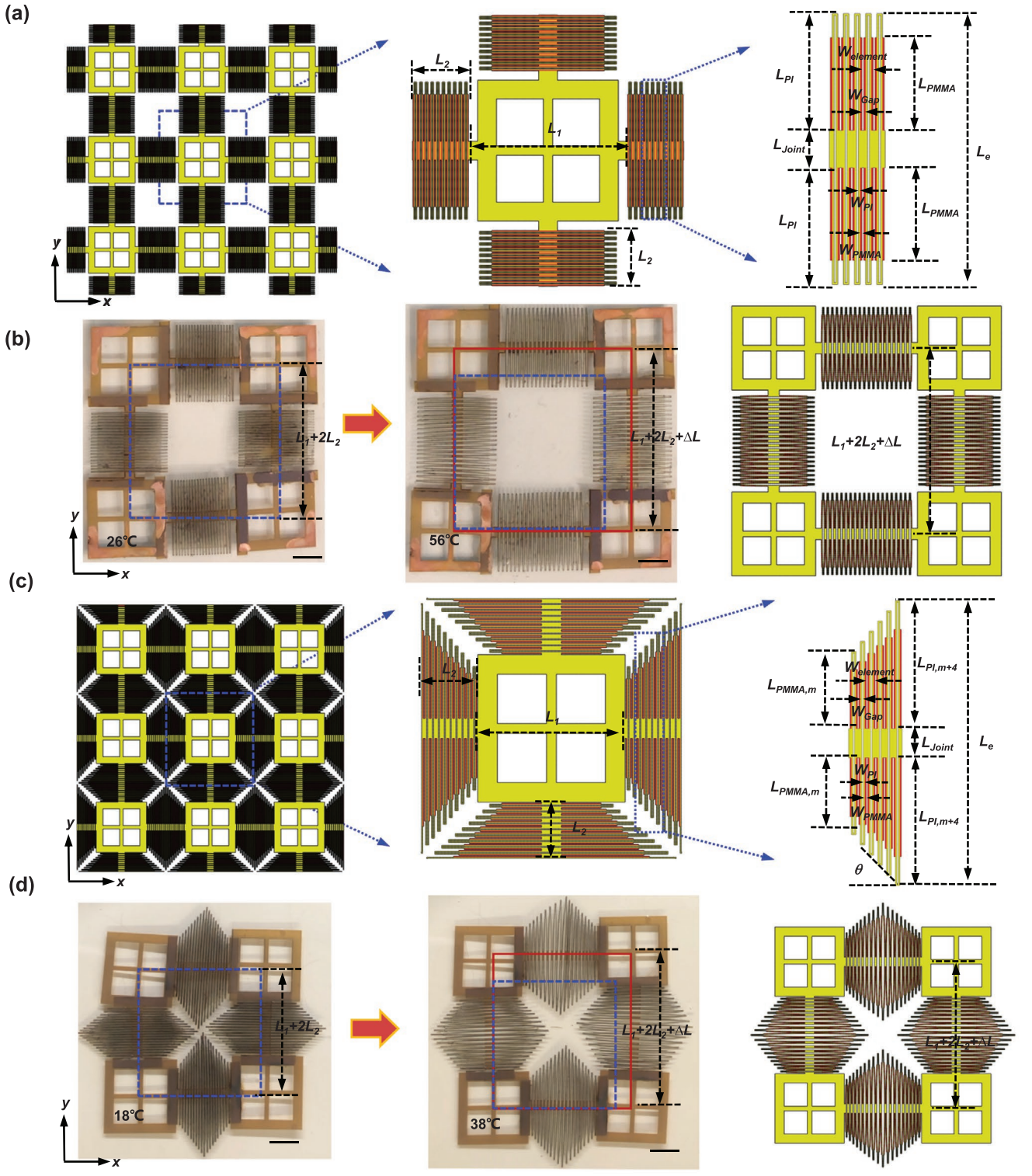

Figure 1. Design strategies and experimental demonstrations of kirigami-inspired 2D hierarchical metamaterials with giant positive thermal expansion. a) Illustration of the hierarchical design and key geometric parameters. b) Optical images of a fabricated metamaterial specimen before (left) and after (middle) a 30 °C increase, along with the deformed configuration predicted by FEA (right). The design parameters include (L_e/L_1, L_{PI}/W_{PI}, L_{PMMA}/L_{PI}, L_2/L_1, W_{PI}/W_{PMMA}, W_{PI}/W_{Gap}, L_1, L_{Joint}, and W_{PI}) = (0.86, 62.8, 0.8, 0.35, 1, 1, 15 mm, 2 mm, and 100 μm). c) Illustration of the hierarchical design with a gradient in the vertical length of the fundamental actuating element, and corresponding geometric parameters. d) Optical images of a fabricated metamaterial specimen before (left) and after (middle) a 20 °C increase, along with the deformed configuration predicted by FEA (right). The design parameters include ($L_{e,1}/L_1$, $L_{PI,1}/W_{PI}$, L_{PMMA}/L_{PI}, L_2/L_1, W_{PI}/W_{PMMA}, W_{PI}/W_{Gap}, L_1, L_{Joint}, and W_{PI}) = (0.84, 52.8, 0.8, 0.37, 1, 1, 15 mm, 2 mm, and 100 μm). Scale bars: 5 mm.

same geometric configuration of the structural branches in Figure 1b undergoes a considerable uniaxial thermal expansion strain (≈45.6%), upon a 40 °C temperature increase (from 25 to 65 °C). This deformation corresponds to an effective CTE of $\alpha_{meta,e} = \Delta L/(L_0\Delta T) = 10\,080$ ppm K^{-1}, which is around 144 times larger than the CTE (α_{PMMA}) of the constituent material (PMMA).

Figure 1c presents a variant of this design that exploits a linear gradient in the total vertical length of the fundamental actuating element to further enhance the effective CTE as well as the filling ratio. In particular, the vertical length (L_e) follows a stepwise increment of $2W_{element}\tan(\theta)$, where $W_{element}$, the width of a fundamental actuating element, is given by $2W_{PI} + 2W_{PMMA} + 2W_{Gap}$, and θ is the slant angle of the actuating element. Figure 1d summarizes experimental and FEA results for thermal expansion in a typical specimen with this type of design, with $W_{PMMA}/W_{PI} = 1$, $W_{Gap}/W_{PI} = 1$, $L_{PI}/W_{PI} = 52.8$, $L_{PMMA}/L_{PI} = 0.8$, $L_{e,1}/L_1 = 0.84$, $L_2/L_1 = 0.37$, $\theta = 49°$, $L_{Joint} = 2$ mm, and $W_{PI} = 100$ µm. Here, $L_{e,1}$ is the vertical length of the fundamental actuating element closely adjacent to the central base. This specimen gives rise to a biaxial thermal expansion of ≈ 21.4% for 20 °C increase, corresponding to an isotropic effective CTE of $\alpha_{meta,h} = 10\,710$ ppm K^{-1} $= 153\alpha_{PMMA}$. Such an improvement of CTE mainly follows from the use of a larger length-to-width ratio (L_{PI}/W_{PI}) that results in an increased bending deflection, when the other geometric parameters are fixed.

A theoretical model of thermal expansion can serve as the basis for designs to achieve a broad range of desirable CTE. Considering the periodicity of kirigami-inspired actuating elements (Figure 1a), we only need to study the thermally induced deformations in a fundamental actuating element (Figure S3(a), Supporting Information). This structure can be modeled as two bilayer beams (consisting of frame and actuation materials) connected at two ends, which can be approximated as clamped boundaries at two ends. Due to the structural symmetry, only a single bilayer beam is analyzed, as shown in Figure S3(b), Supporting Information, where the bending moment (M) corresponds to the only non-zero component of generalized inner forces at two ends. Then the thermally induced deformations can be analyzed by considering a two-step process, that is, thermally induced bending in a free-standing bilayer beam without any constraints, and mechanical deformations induced by the application of a pair of bending moments to ensure zero rotational angles at the two ends of the bilayer beam. In the framework of small deflections, the vertical displacement at the middle of the bilayer beam can be given by (see Note S1, Supporting Information, for details)

$$y_M = \int_0^{\theta_{s^*}} \sin\theta \frac{d\theta}{\sqrt[2]{\left(K - \frac{M}{E_b I_b}\right)^2}} - \int_{\theta_{s^*}}^{0} \sin\theta \frac{d\theta}{\sqrt[2]{\left(\frac{M}{E_f I_f}\right)^2}} + \left(y_0 - \frac{w_f}{2}\right)\cos(\theta_{s^*}) - \left(y_0 - \frac{w_f}{2}\right) \quad (1)$$

Here, E_bI_b and E_fI_f are the bending stiffness of the bilayer and frame layer, respectively. K and y_0 are the curvature and the location of the neutral mechanical plane of the bilayer beam during the thermally induced bending, respectively, and are expressed as

$$K = \frac{6(W_f + W_a)\Delta T\Delta\alpha}{4W_f^2 + 4W_a^2 + 6W_f w_a + E_f W_f^3/E_a W_a + E_a W_a^3/E_f W_f} \quad (2a)$$

$$y_0 = \frac{(E_f\alpha_f W_f + E_a\alpha_a W_a)\Delta T/K + \frac{1}{2}E_f W_f^2 + \frac{1}{2}E_a W_a^2 + E_a W_f W_a}{E_f W_f + E_a W_a} \quad (2b)$$

where E_a and w_a are the elastic modulus and width of actuation layer, while E_f and w_f are the elastic modulus and width of the frame layer. In comparison to the bending deflections, the change of the total length of the bilayer beam can be neglected. As such, the rotational angle θ_{s^*} at $(L_e - L_a)/2$ (see Note S1, Supporting Information, for details) and the bending moment (M) can be determined numerically by solving the following equation using the random searching algorithm (RSA),

$$L_s = \int_0^{\theta_{s^*}} \frac{d\theta}{\sqrt[2]{\left(K - \frac{M}{E_b I_b}\right)^2}} - \int_{\theta_{s^*}}^{0} \frac{d\theta}{\sqrt[2]{\left(\frac{M}{E_f I_f}\right)^2}} \quad (3)$$

Here, L_a and L_s are the lengths of actuation material and the deformed bilayer beam. With solved θ_{s^*} and M, the vertical displacement y_M in Equation (1) can be calculated. The effective thermal expansion coefficient ($\alpha_{meta,e}$) of a fundamental actuating element can be then obtained as

$$\alpha_{meta,e} = \frac{2y_M}{W_{element}} \quad (4)$$

Notably, materials with a large difference in CTE and an optimal value of modulus ratio (i.e., $E_a/E_f = 2$) represent optimized choices for kirigami-inspired hierarchical metamaterials designed for large thermal expansion or shrinkage (Figure S4, Supporting Information). For the fundamental actuating element composed of PI (i.e., frame material) and PMMA (i.e., actuation material) ($E_{PI}/E_{PMMA} = 1$, $\alpha_{PMMA} = 70$ ppm K^{-1}, and $\alpha_{PI} = 30$ ppm K^{-1}), adopted in the current experiment, the predictions derived from Equation (1)–(4) agree reasonably well with FEA results for a range of different geometric parameters (Figure S3(d), Supporting Information), providing quantitative evidence for the accuracy of the developed theoretical model. According to this model, the CTE ($\alpha_{meta,e}$) of the proposed metamaterial design can be tuned in a broad range, by varying the four non-dimensional geometric parameters, including W_{PMMA}/W_{PI}, W_{Gap}/W_{PI}, L_{PI}/W_{PI}, and L_{PMMA}/L_{PI}, as to be shown subsequently.

Figure 2a depicts the contour plot of the magnification factor of CTE, $\lambda = \alpha_{meta,e}/\alpha_{PMMA}$, with respect to L_{PI}/W_{PI} and L_{PMMA}/L_{PI}, while fixing the other geometric parameters as $W_{PMMA}/W_{PI} = W_{Gap}/W_{PI} = 1$, and $L_{Joint}/W_{PI} = 20$. As evidenced by the excellent agreement between theoretical predictions and experimental/FEA results, λ increases as the length ratio L_{PMMA}/L_{PI} increases initially, until it reaches its

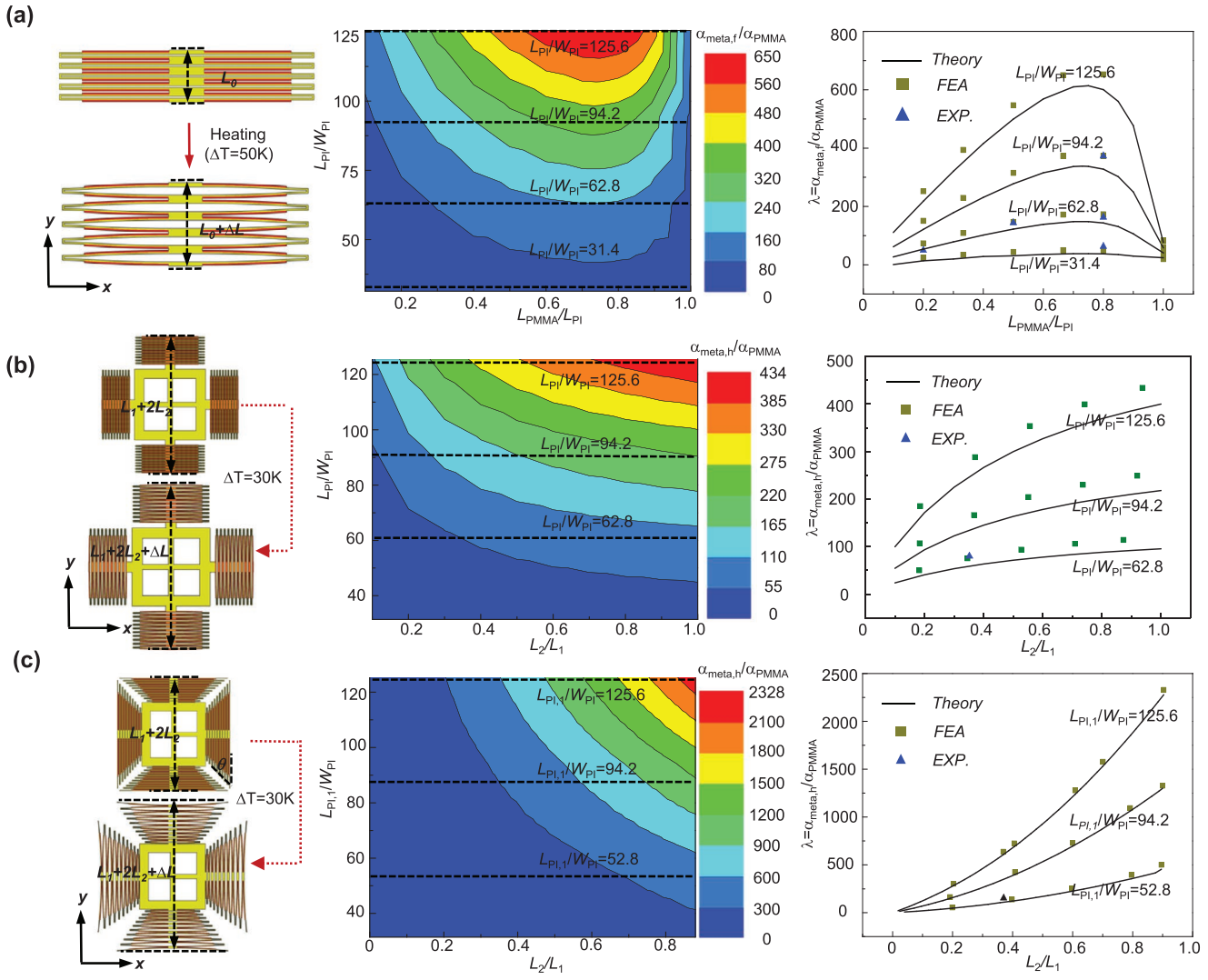

Figure 2. Microstructure–property relationship of kirigami-inspired 2D hierarchical designs with positive thermal expansion. a) Illustration of the fundamental actuating element (left), contour plot of the simulated magnification factor of CTE in terms of L_{PI}/W_{PI} and L_{PMMA}/L_{PI} (middle), and magnification factor of CTE versus L_{PMMA}/L_{PI} for four different L_{PI}/W_{PI} (right). The other parameters are fixed as L_{Joint} = 2 mm and W_{PI} = W_{PI} = W_{PI} = 100 µm. b) Illustration of the 2D hierarchical metamaterial (left), contour plot of the simulated magnification factor of CTE in terms of L_2/L_1 and L_{PI}/W_{PI} (middle), and magnification factor of CTE versus L_1/L_2 for three different L_{PI}/W_{PI} (right). The other parameters are fixed as L_{Joint} = 2 mm, W_{PI} = W_{PI} = W_{PI} = 100 µm, L_1 = 15 mm, L_e/L_1 = 0.86, and L_{PMMA}/L_{PI} = 0.8. c) Illustration of the 2D hierarchical metamaterial with a gradient design (left), contour plot of the simulated magnification factor of CTE in terms of L_2/L_1 and $L_{PI,1}/W_{PI}$ (middle), and the magnification factor of CTE versus L_1/L_2 for three different $L_{PI,1}$/WPI (right). The other parameters are fixed as L_{Joint} = 2 mm, W_{PI} = W_{PI} = W_{PI} = 100 µm, $L_{e,1}/L_1$ = 0.84, and L_{PMMA}/L_{PI} = 0.8.

peak value (≈650 for L_{PI}/W_{PI} = 125.6) at ≈ 0.75, beyond which λ decreases, due to the constraint at the joints of the bilayer beams. By contrast, λ increases monotonously with increasing L_{PI}/W_{PI} (Figure 2a and Figure S5(a), Supporting Information). In particular, the simulated uniaxial CTE ($\alpha_{meta,e}$) of the fundamental actuating element reaches 25 900 ppm K^{-1} for L_{PMMA}/L_{PI} = 0.8 and L_{PI}/W_{PI} = 94.2, which is in good agreement with experiment (26 110 ppm K^{-1}). The effect of the width ratio W_{PMMA}/W_{PI} on λ is also investigated (Figure S5(b), Supporting Information). Similar to the dependence on L_{PMMA}/L_{PI}, λ also reaches its maximum at an optimal width ratio (i.e., W_{PMMA}/W_{PI} = 0.75), beyond the value reduces slightly with the further increase of width ratio. Since λ shows small correlation with the width ratio in the range of [0.75, 1.0], the widths of PI, PMMA, and gap are all fixed as 100 µm in the experimental study, considering the resolution of laser cutting technique. The results in Figure 2a and Figure S5, Supporting Information, suggest the length ratio (L_{PMMA}/L_{PI}) and length-to-width ratio (L_{PI}/W_{PI}) as the two dominant geometric parameters that affect the effective CTE. For the typical range of temperature increase (from room temperature to 200 K), the thermal strain of the fundamental actuating element increases proportionally as the temperature increases (Figure S6, Supporting Information), thereby yielding a constant CTE. Such a linear thermal expansion behavior is beneficial for the precise control of thermal deformations. By considering the plastic yielding of the constituent materials and using 1% as the yield strain for both PI and PMMA, we can estimate the value of maximum thermal

expansion in the mechanical metamaterial. FEA results show that the maximum thermal expansion of the fundamental kirigami element increases rapidly with increasing length to width ratio L_{PI}/W_{PI}, from 37% for $L_{PI}/W_{PI} = 25$ to 568% for $L_{PI}/W_{PI} = 125.6$ (Figure S7, Supporting Information).

Figure 2b presents the results of experimental measurement, theoretical modeling, and FEA for the 2D hierarchical metamaterial consisting of a square base (PI, length L_1) in the center. As compared to the thermal deformations of structural branches, the thermal expansion of the square base can be neglected. Therefore, the effective CTE ($\alpha_{meta,h}$) of the hierarchical metamaterial can be approximately related to the CTE ($\alpha_{meta,e}$) of the fundamental actuating element in structural branches by

$$\alpha_{meta,h} = \alpha_{meta,e} \frac{2(L_2/L_1)}{1+2(L_2/L_1)} \quad (5)$$

The contour plot in Figure 2b summarizes FEA results for λ in terms of L_2/L_1 and L_{PI}/W_{PI}, with fixed $L_{PMMA}/L_{PI} = 0.8$, $W_{PMMA}/W_{PI} = W_{Gap}/W_{PI} = 1$, $L_e/L_1 = 0.86$, and $L_{Joint}/W_{PI} = 20$. The dependence is similar to that of the fundamental actuating element in Figure 2a, while λ is reduced slightly, due to the presence of a square base. In this case, the thermal expansion of the metamaterial is biaxial, and the simulated CTE ($\alpha_{meta,h}$) reaches 5250 ppm K^{-1} for $L_2/L_1 = 0.35$ and $L_{PI}/W_{PI} = 62.8$, agreeing well with the experimental measurement (5600 ppm K^{-1}). Figure 2c provides the results of CTE for the hierarchical metamaterial with a gradient in the vertical length of the fundamental actuating element. Here, the slant angle (θ) of the actuating element represents an additional design parameter. Under the geometric constraint that the self-overlap does not occur, the CTE ($\alpha_{meta,h}$) increases monotonously with increasing the slant angle (Figure S8, Supporting Information). For a fixed slant angle ($\theta = 49°$), the dependence of $\alpha_{meta,h}$ on the geometric parameters ($L_{PI,1}/W_{PI}$ and L_2/L_1) is shown in the middle and right of Figure 2c, where $L_{PI,1}$ is the length of the PI layer in the fundamental actuating element closely adjacent to the central base. Evidence of improvement of the CTE can be observed in comparison to the design (Figure 2b) without the length gradient in the actuating element. For example, the gradient design with a slant angle of 49° gives rise to 2.6-fold enhancement (relatively) of CTE for $L_2/L_1 = 0.4$ and $L_{PI}/W_{PI} = 94.2$. It is noteworthy that a giant biaxial CTE of 10 710 ppm K^{-1} (9660 ppm K^{-1} based on FEA) has been demonstrated experimentally for $L_{PI,1}/W_{PI} = 52.8$ and $L_2/L_1 = 0.4$, which is an order of magnitude larger than the largest experimental results (up to ≈ 1050 ppm K^{-1}) of biaxial CTE reported in previous studies.[12] The excellent agreement among simulations, experiments, and theoretical predictions suggest the theoretical model as a reliable reference for the design of the kirigami-inspired hierarchical metamaterial in achieving a desired positive CTE.

Modifications of the fundamental actuating elements by switching the actuation material (PMMA) to the other side of frame support (PI) allow access to a range of tunable negative CTE. **Figure 3**a shows such a design that shrinks upon a 10 °C temperature increase, which mainly arises from the change of bending direction in the PMMA/PI bilayer beam. The middle and right panels present the optical images of the specimen ($L_{PMMA}/L_{PI} = 0.8$ and $L_{PI}/W_{PI} = 62.8$) before and after a 10 °C heating. The thermal shrinkage is around 11.6%, corresponding to an effective negative CTE of –11550 ppm K^{-1}. Due to the same deformation mechanisms, the magnitude of negative CTE can also be analyzed theoretically, according to Equations (1) and (4). As evidenced by both the results of the theoretical model and experimental measurement, λ of the fundamental actuating element exhibits a similar non-monotonic dependence on the length ratio (L_{PMMA}/L_{PI}) and width ratio (W_{PMMA}/W_{PI}) (Figure 3d and Figure S9, Supporting Information), as compared to the aforementioned metamaterial design with positive CTE. In this case, the length ratio (L_{PMMA}/L_{PI}) and length-to-width ratio (L_{PI}/W_{PI}) still represent the two primary geometric parameters to yield a broad range of desired negative CTE. Combined theoretical modeling, FEA and experiments establish design principles for mechanical metamaterials that yield desired negative CTE values. In particular, a length-to-width ratio (L_{PI}/W_{PI}), as well as an optimal value of length ratio (L_{PMMA}/L_{PI}) and width ratio (W_{PMMA}/W_{PI}) are preferred to offer a large negative thermal deformation.

Figure 3b presents a representative design of a 2D kirigami-inspired hierarchical metamaterial that interconnects the fundamental actuating elements with a square base in the center. Here, the geometric parameters include $L_{PMMA}/L_{PI} = 0.8$, $L_{PI}/W_{PI} = 52.8$, $L_1/L_e = 1.2$, and $L_2/L_1 = 0.4$. The resulting biaxial CTE ($\alpha_{meta,h}$) is –4550 ppm K^{-1} according to the experiments, and –3920 ppm K^{-1} according to FEA. The considerable thermal shrinkage after a 10 °C heating reveals a giant absolute value of biaxial negative CTE. Dependence of the CTE on the key geometric parameters is illustrated in Figure S10, Supporting Information. Figure 3c depicts a hierarchical metamaterial design with a gradient pattern of actuating elements, with $L_{PMMA}/L_{PI} = 0.8$, $L_{PI,1}/W_{PI} = 52.8$, $L_2/L_1 = 0.38$, $L_1/L_{e,1} = 1.2$, and $\theta = 15°$. Such a gradient pattern results in an enhanced negative CTE, as evidenced by the experiments (–5950 ppm K^{-1}) and FEA (–5600 ppm K^{-1}), which substantially exceeds those (up to –966 ppm K^{-1}) reported in previous experiments.[12] Figure 3e and f shows that a larger absolute value of negative CTE can be achieved by adopting a higher length ratio (L_2/L_1) or length-to-width ratio (L_{PI}/W_{PI} or $L_{PI,1}/W_{PI}$). By integrating the two different fundamental actuating elements (Figure 2a and Figure 3a) along the different directions of the hierarchical metamaterial, anisotropic thermal expansion with positive CTE along the *x*-direction and negative CTE along the *y*-direction can be achieved, as illustrated in Figure S11, Supporting Information. Additional experimental details of the uniaxial and biaxial thermal deformation of 2D hierarchical metamaterials can be found in Movies S1–S5, Supporting Information. In addition, we qualitatively and quantitatively investigated the performance of kirigami-inspired 2D hierarchical designs during thermal cycles (Figure S12, Supporting Information). A stable response of CTE can be observed in the experiment during 10 thermal cycles, and no structural fracture occurs. These observations are supported by the FEA results (Figure S12a, Supporting Information), where the maximum principal strains (0.085%) of PI and PMMA are both far below the yield strain (1% for PI and PMMA) of these constituent materials.

Figure 4 provides an Ashby plot of CTE versus density that covers the systems reported here, along with mechanical

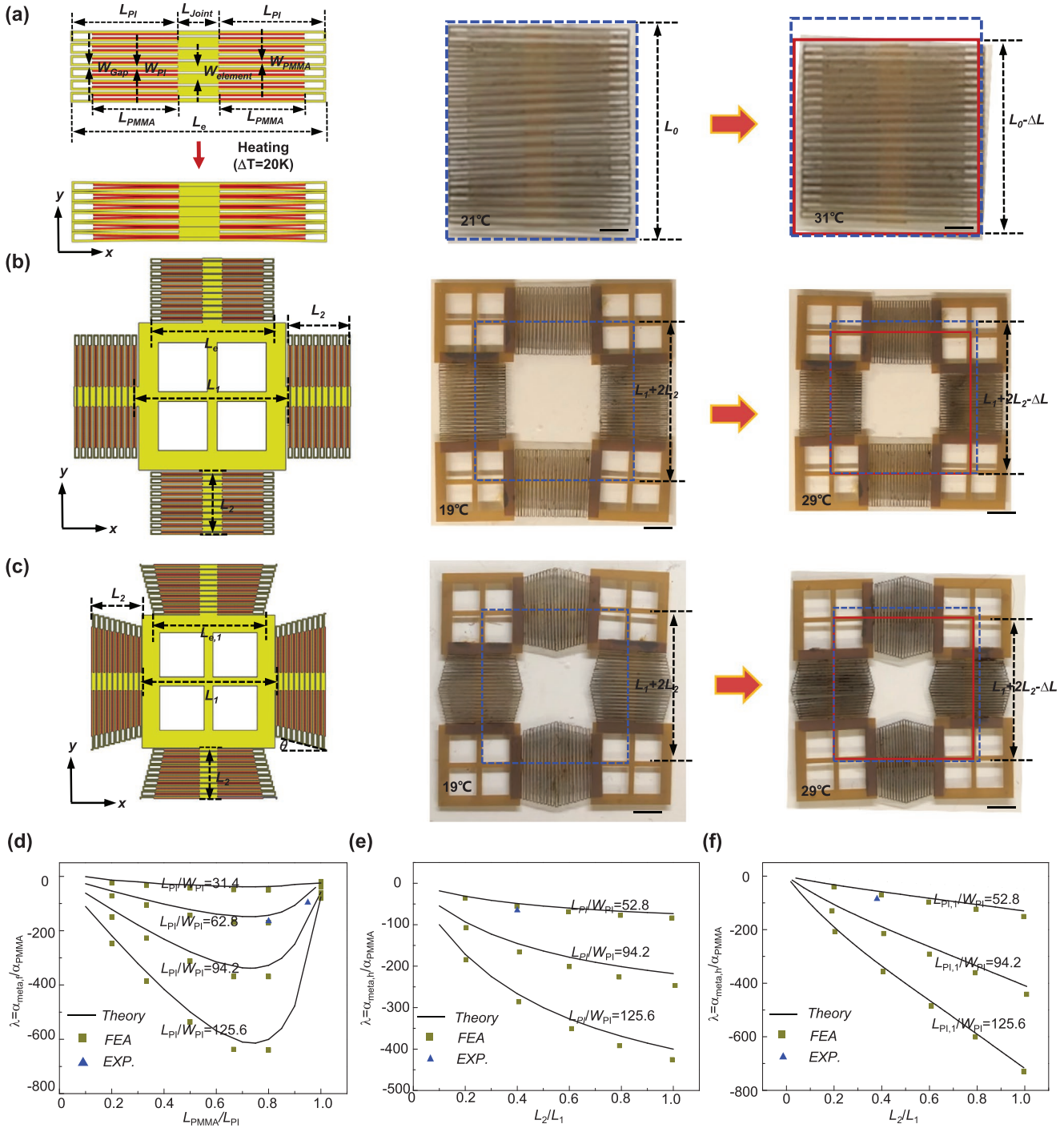

Figure 3. Design strategies, experimental demonstration, and microstructure–property relationship of kirigami-inspired 2D hierarchical designs with negative thermal expansion. a) Illustration of the fundamental actuating element (left), and optical images of a fabricated specimen before (middle) and after (right) undergoing a 10 °C increase. The design parameters include (L_{PI}/W_{PI}, L_{PMMA}/L_{PI}, W_{PI}/W_{PMMA}, W_{PI}/W_{gap}, L_1, L_{Joint}, and W_{PI}) = (62.8, 0.8, 1, 1, 15 mm, 2 mm, and 100 μm). b) Illustration of the 2D hierarchical metamaterial (left), and optical images of a fabricated metamaterial specimen before (middle) and after (right) undergoing a 10 °C increase. The design parameters include (L_1/L_e, L_{PI}/W_{PI}, L_{PMMA}/L_{PI}, L_2/L_1, W_{PI}/W_{PMMA}, W_{PI}/W_{Gap}, L_1, L_{Joint}, and W_{PI}) = (1.2, 52.8, 0.8, 0.4, 1, 1, 15 mm, 2 mm, and 100 μm). c) Illustration of the 2D hierarchical metamaterial with a gradient design (left), and optical images of a fabricated metamaterial specimen before (middle) and after (right) undergoing a 10 °C increase. The design parameters include ($L_1/L_{e,1}$, $L_{PI,1}/W_{PI}$, L_{PMMA}/L_{PI}, L_2/L_1, W_{PI}/W_{PMMA}, W_{PI}/W_{Gap}, L_1, L_{Joint}, and W_{PI}) = (1.2, 52.8, 0.8, 0.4, 1, 1, 15 mm, 2 mm, and 100 μm). d) Magnification factor of CTE versus L_{PMMA}/L_{PI} for the fundamental actuating element with four different L_{PI}/W_{PI} and fixed L_{Joint} = 2 mm and $W_{PMMA} = W_{PI} = W_{Gap}$ = 100 μm. e,f) Magnification factor of CTE versus L_1/L_2 for the 2D hierarchical metamaterials in (b) and (c) with three different L_{PI}/W_{PI} or $L_{PI,1}/W_{PI}$. The other parameters are fixed as L_{Joint} = 2 mm, $W_{PMMA} = W_{PI} = W_{Gap}$ = 100 μm, $L_1/L_e = L_1/L_{e,1} = 1.2$, and L_{PMMA}/L_{PI} = 0.8. Scale bars: 5 mm.

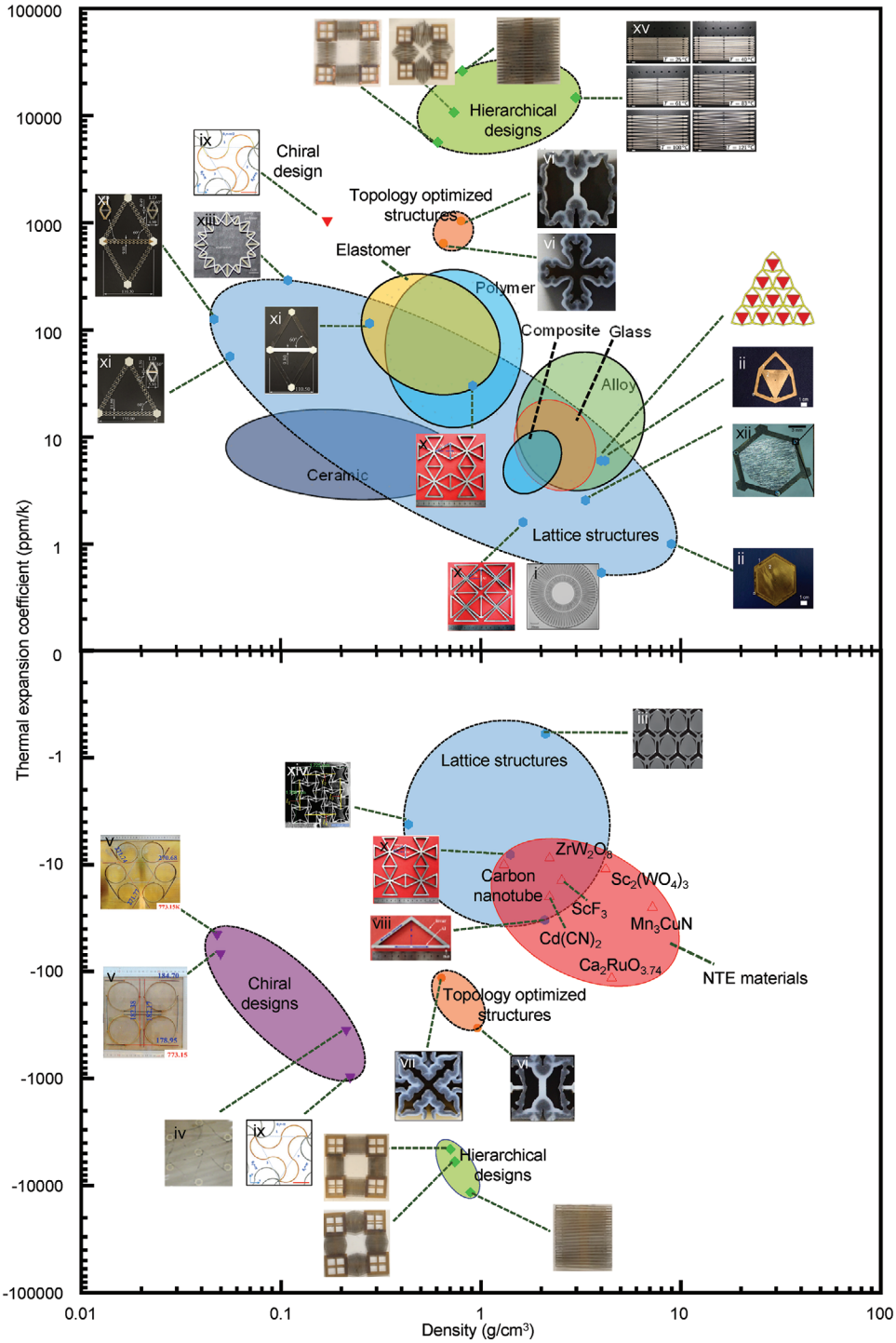

Figure 4. Ashby plot of the thermal expansion coefficients of natural materials,[11,64] NTE materials,[50,52,72–77] representative mechanical metamaterials reported previously (i.e., planar lattice structures,[3–5,11,54,56,60,61,63,66] topology optimized structures,[9,10] and chiral metamaterials[6,7,12]), and kirigami-inspired 2D hierarchical designs proposed in the previous[70] and current work. i) Reproduced with permission.[3] Copyright 2018, Elsevier Ltd. ii) Reproduced with permission.[4] Copyright 2011, Elsevier B.V. iii) Reproduced with permission.[5] Copyright 2014, Wiley-VCH. iv) Reproduced with permission.[6] Copyright 2015, Wiley-VCH. v) Reproduced with permission.[7] Copyright 2016, American Chemical Society. vi) Reproduced with permission.[9] Copyright 2017, Elsevier Ltd. vii) Reproduced under the terms of the CC-BY Creative Commons Attribution 3.0 Unported license (https://creativecommons.org/licenses/by/3.0).[10] Copyright 2015, The Authors, published by American Institute of Physics. viii) Reproduced with permission.[11] Copyright 2017, ASME. ix) Reproduced with permission.[12] Copyright 2019, Wiley-VCH. x) Reproduced with permission.[54] Copyright 2015, Elsevier Ltd. xi) Reproduced with permission.[56] Copyright 2017, Acta Materialia Inc. xii) Reproduced with permission.[60] Copyright 2013, Springer Nature. xiii) Reproduced with permission.[61] Copyright 2018, Elsevier Ltd. xiv) Reproduced with permission.[66] Copyright 2019, Elsevier Ltd. xv) Reproduced with permission.[70] Copyright 2019, Elsevier Ltd.

metamaterials reported previously and collections of natural and engineering materials. The results focus on experimental demonstrations, noting that many designs demonstrated only through FEA or theoretical modeling are not practicable in fabrication (e.g., because of extreme geometric layouts). For most natural and engineering materials, including metals, polymers, elastomers, and glasses, the CTE falls into a narrow positive range, from ≈1 to 300 ppm K^{-1}.[11,64] Of the mechanical metamaterials demonstrated previously, traditional 2D lattice designs constructed with straight ribbons and rigid plates patterned in

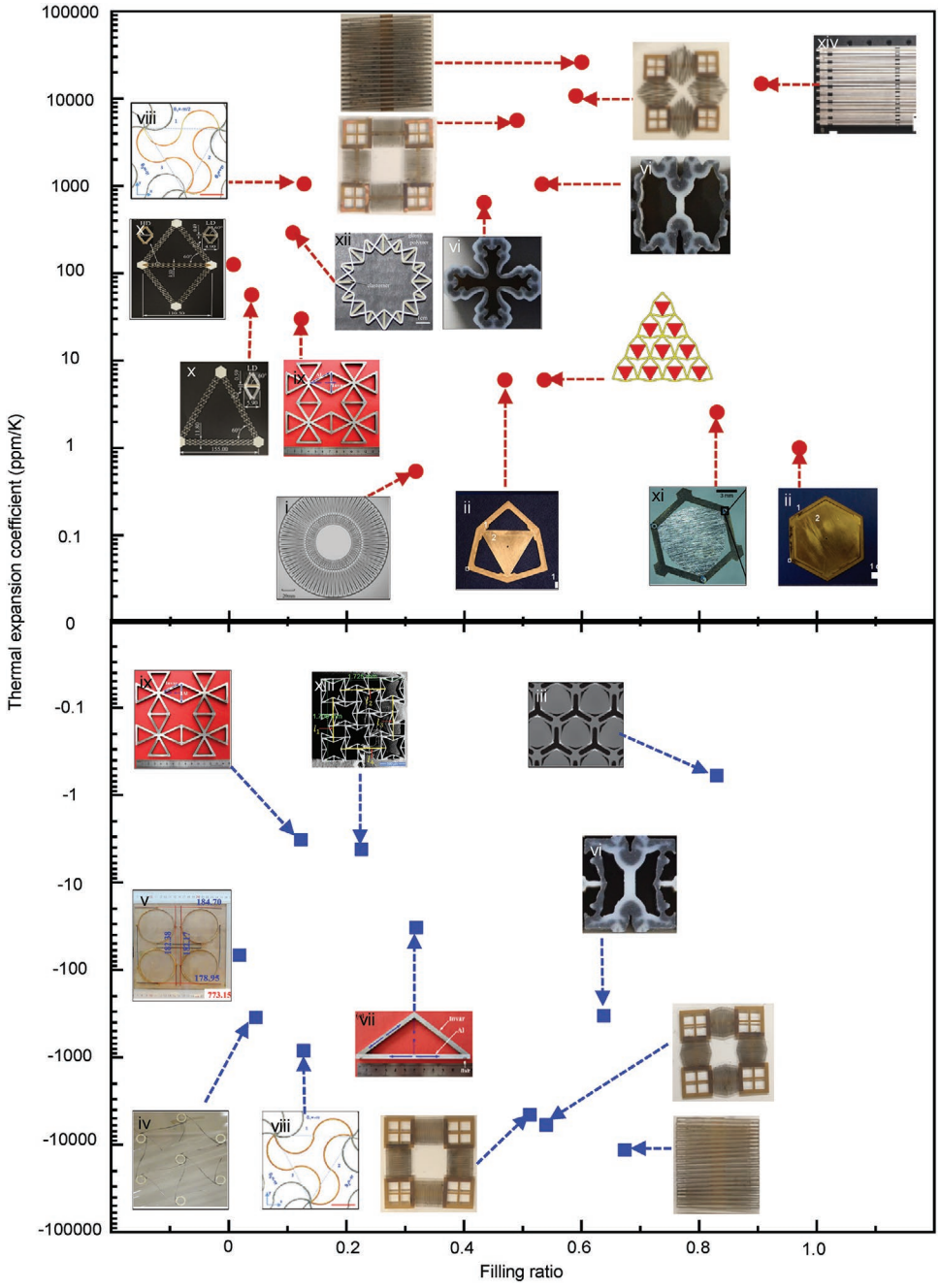

Figure 5. Ashby plot of the thermal expansion coefficients versus the filling ratio for the representative mechanical metamaterials reported previously[3–7,9–12,54,56,60,61,63,66,70] and kirigami-inspired 2D hierarchical designs proposed in the current work. i) Reproduced with permission.[3] Copyright 2018, Elsevier Ltd. ii) Reproduced with permission.[4] Copyright 2011, Elsevier B.V. iii) Reproduced with permission.[5] Copyright 2014, Wiley-VCH. iv) Reproduced with permission.[6] Copyright 2015, Wiley-VCH. v) Reproduced with permission.[7] Copyright 2016, American Chemical Society. vi) Reproduced with permission.[9] Copyright 2017, Elsevier Ltd. vii) Reproduced with permission.[11] Copyright 2017, ASME. viii) Reproduced with permission.[12] Copyright 2019, Wiley-VCH. ix) Reproduced with permission.[54] Copyright 2015, Elsevier Ltd. x) Reproduced with permission.[56] Copyright 2017, Acta Materialia Inc. xi) Reproduced with permission.[60] Copyright 2013, Springer Nature. xii) Reproduced with permission.[61] Copyright 2018, Elsevier Ltd. xiii) Reproduced with permission.[66] Copyright 2019, Elsevier Ltd. xiv) Reproduced with permission.[70] Copyright 2019, Elsevier Ltd.

different topologies (e.g., triangular, honeycomb, star, etc.) are among the most extensively studied.[3–5,11,54,56,60,61,63,66] These metamaterials can serve as a robust tunable platform to render either close-to-zero CTE, or large positive/negative CTE (up to 290 ppm K^{-1} and down to −33 ppm K^{-1}, respectively). Advanced 3D printing technologies allow fabrication of mechanical metamaterials consisting of different engineering materials, but with complex 3D architectures designed through topology optimization.[9,10] This type of metamaterials can be tailored to offer either large positive CTE (up to ≈1040 ppm K^{-1}) or negative CTE (down to −335 ppm K^{-1}), but limitations of 3D printing techniques in terms of fabrication resolution and available material types set constraints on practical applications, and on strategies to further broaden the range of accessible CTE. To enable a large magnitude of negative CTE, a certain class of mechanical metamaterials (also referred to as "chiral mechanical metamaterials") relies on the rotations of straight or curved beams in periodic unit cells is systematically studied, where the reported CTE can reach −966 ppm K^{-1}.[6,7,12] To summarize, existing experimental results on mechanical metamaterials cover a range of [−966, 1050 ppm K^{-1}] for biaxial CTE. The kirigami-inspired 2D hierarchical metamaterials in the current study significantly expand this range to [−5950 to 10 710 ppm K^{-1}]. Both negative and positive uniaxial CTEs (i.e., −11 550 and 26 110 ppm K^{-1}) demonstrated herein also establish a record, noting that the largest positive uniaxial CTE[70] reported previously is 14 700 ppm K^{-1}.

The combined capabilities in a broad tunable CTE range, a large controllable thermal expansion, and a high filling ratio could be useful to match the thermal deformations of surrounding components, especially for large environmental temperature changes. **Figure 5** and Figure S13, Supporting Information, summarize the filling ratios and feature sizes of existing mechanical metamaterials, noting that reductions in feature sizes can result in improvements in thermal response times. Although the triangular and hexagonal lattice structures consisting of inner triangular/hexagonal plates and straight ribbons possess very high filling ratios (e.g., from 0.47 to 0.97), the designs focus on close-to-zero thermal expansion. The chiral mechanical metamaterials usually leverage relatively slender ribbons and hollow circular nodes to induce large negative CTE, which leads to very low filling ratios (e.g., <0.2) as well. In comparison, the kirigami-inspired hierarchical designs presented here provide robust routes to mechanical metamaterials that combine high filling ratios (>0.5) and an unprecedented range of CTE. As demonstrated previously, the response time decreases with the decrease of the thickness of 2D mechanical metamaterials with filamentary microstructures.[12] In the current study, the manufacturing technologies of drop-casting, laser cutting, and wet etching allow reliable formation of metamaterials with lateral feature sizes down to 100 µm (Figure S13, Supporting Information), thereby with capabilities of relatively quick responses (i.e., response time <1 s for microstructures with 100 µm width and 75 µm thickness) upon a change in temperature.

In conclusion, we report a type of 2D hierarchical metamaterial design that incorporates kirigami-inspired bilayer actuating elements into periodic lattice patterns. As evidenced by the agreement between theoretical modeling, FEA simulations, and experimental measurements, these systems can be tailored precisely to offer a broad range of CTE, including large isotropic/anisotropic thermal expansion or shrinkage in a linear mode. Quantitative comparison of the thermal expansion responses to the previously reported mechanical metamaterials suggests that the results reported here substantially enlarge the accessible range of CTE in the Ashby plot, by nearly an order of magnitude for biaxial CTE. The combined attributes of exceptional isotropic/anisotropic CTEs, large thermal deformations with linear behavior, high filling ratios, and relative fast thermal responses offer potentially powerful options for applications in deployable systems in aerospace, shape morphing structures, biomedical devices, thermal switches and actuators, optical devices, and others that demand operations in a broad range of temperatures.

Experimental Section

Fabrication of the Metamaterials: The fabrication process started with a Cu–PI sheet (75-µm-thick middle PI layer, 18-µm-thick top and bottom Cu layer, AP8535R, DuPont Pyralux). After removing the top Cu layer using wet etching (CE-100 copper etchant, Transense, 15 min), four pieces of water-soluble tape (OKI-AKW WT-1, Aquasol) was attached to the bottom surface. An ultraviolet laser cutter (ProtoLaser U4, LPKF) removed selected regions of PI. PMMA (495 PMMA A5, Microchem) infilled the patterned PI structures. A mechanical polisher removed the top layer of PMMA. Aligned laser cutting defined the outer contours of the sample. Rinsing the sample with deionized (DI) water removed the water-soluble tape and wet etching removed the Cu layer.

Finite-Element Analysis (FEA): Simulations of the thermal responses upon a temperature increase were conducted using the commercial software ABAQUS. Four-node shell (S4R) elements with refined meshes allowed modeling of kirigami-inspired 2D hierarchical structures with testified accuracy. The elastic modulus, Poisson's ratio, and CTE were 3 GPa, 0.34, and 30 ppm K^{-1} for PI, and 3 GPa, 0.3, and 70 ppm K^{-1} for PMMA, respectively.

Supporting Information

Supporting Information is available from the Wiley Online Library or from the author.

Acknowledgements

X.G., X.N., and J.L. contributed equally to this work. This work was supported by a grant from the Institute for Guo Qiang, Tsinghua University (Grant No. 2019GQG1012). Y.Z. acknowledges support from the National Natural Science Foundation of China (Grant Nos. 11722217 and 11921002), the Tsinghua University Initiative Scientific Research Program (Grant No. 2019Z08QCX10), the Tsinghua National Laboratory for Information Science and Technology and the Henry Fok Education Foundation. X.G. acknowledges support from National Natural Science Foundation of China (Grant No. 11702155). Y.H. acknowledges support from the NSF (Grant No. CMMI1635443). X.N. and J.A.R. acknowledge support from the ARO MURI program. This work made use of the EPIC facility of Northwestern University's NUANCE Center, which has received support from the SHyNE Resource (NSF ECCS-2025633), the IIN, and Northwestern's MRSEC program (NSF DMR-1720139).

Conflict of Interest

The authors declare no conflict of interest.

Keywords

giant positive and negative CTEs, hierarchical structures, kirigami designs, mechanical metamaterials, unusual thermal responses

Received: July 19, 2020
Revised: September 14, 2020
Published online: December 2, 2020

[1] C. A. Steeves, S. L. dos Santos e Lucato, M. He, E. Antinucci, J. W. Hutchinson, A. G. Evans, *J. Mech. Phys. Solids* **2007**, *55*, 1803.
[2] J. Berger, C. Mercer, R. M. McMeeking, A. G. Evans, *J. Am. Chem. Soc.* **2011**, *94*, S42.
[3] Y. Xie, X. Pei, J. Yu, *Compos. Struct.* **2018**, *203*, 709.
[4] R. K. Rhein, M. D. Novak, C. G. Levi, T. M. Pollock, *Mater. Sci. Eng. A* **2011**, *528*, 3973.
[5] N. Yamamoto, E. Gdoutos, R. Toda, V. White, H. Manohara, C. Daraio, *Adv. Mater.* **2014**, *26*, 3076.
[6] C. S. Ha, E. Hestekin, J. Li, M. E. Plesha, R. S. Lakes, *Phys. Status Solidi B* **2015**, *252*, 1431.
[7] L. Wu, B. Li, J. Zhou, *ACS Appl. Mater. Interfaces* **2016**, *8*, 17721.
[8] Q. Wang, J. A. Jackson, Q. Ge, J. B. Hopkins, C. M. Spadaccini, N. X. Fang, *Phys. Rev. Lett.* **2016**, *117*, 175901.
[9] A. Takezawa, M. Kobashi, *Composites, Part B* **2017**, *131*, 21.
[10] A. Takezawa, M. Kobashi, M. Kitamura, *APL Mater.* **2015**, *3*, 076103.
[11] K. Wei, Y. Peng, W. Wen, Y. Pei, D. Fang, *J. Appl. Mech.* **2017**, *84*, 101006.
[12] X. Ni, X. Guo, J. Li, Y. Huang, Y. Zhang, J. A. Rogers, *Adv. Mater.* **2019**, *31*, 1905405.
[13] K. Patterson, S. Pellegrino, *Appl. Opt.* **2013**, *52*, 5327.
[14] C. S. Coates, A. L. Goodwin, *Mater. Horiz.* **2019**, *6*, 211.
[15] M. M. Toropova, C. A. Steeves, *Acta Astronaut.* **2015**, *113*, 132.
[16] K. Wei, Y. Peng, K. Wang, S. Duan, X. Yang, W. Wen, *Compos. Struct.* **2018**, *188*, 287.
[17] K. Kuribara, H. Wang, N. Uchiyama, K. Fukuda, T. Yokota, U. Zschieschang, C. Jaye, D. Fischer, H. Klauk, T. Yamamoto, K. Takimiya, M. Ikeda, H. Kuwabara, T. Sekitani, Y. L. Loo, T. Someya, *Nat. Commun.* **2012**, *3*, 723.
[18] M. L. Lifson, M. W. Kim, J. R. Greer, B. J. Kim, *Nano Lett.* **2017**, *17*, 7737.
[19] H. Yang, D. Qi, Z. Liu, B. K. Chandran, T. Wang, J. Yu, X. Chen, *Adv. Mater.* **2016**, *28*, 9175.
[20] W. Kang, M. T. A. Saif, *Adv. Funct. Mater.* **2013**, *23*, 713.
[21] W. Kang, M. T. A. Saif, *J. Micromech. Microeng.* **2011**, *21*, 105017.
[22] B. Xu, A. Akhtar, Y. Liu, H. Chen, W. H. Yeo, S. I. Park, B. Boyce, H. Kim, J. Yu, H. Y. Lai, S. Jung, Y. Zhou, J. Kim, S. Cho, Y. Huang, T. Bretl, J. A. Rogers, *Adv. Mater.* **2016**, *28*, 4462.
[23] S. Han, M. K. Kim, B. Wang, D. S. Wie, S. Wang, C. H. Lee, *Adv. Mater.* **2016**, *28*, 10257.
[24] K. S. Kumar, P. Y. Chen, H. Ren, *Research* **2019**, *2019*, 3018568.
[25] K.-Y. Park, H. Kim, S. Lee, J. Kim, J. Hong, H.-D. Lim, I. Park, K. Kang, *CrystEngComm* **2016**, *18*, 7463.
[26] C. Xu, Z. Ahmad, A. Aryanfar, V. Viswanathan, J. R. Greer, *Proc. Natl. Acad. Sci. U. S. A.* **2017**, *114*, 57.
[27] V. Giordani, D. Tozier, H. Tan, C. M. Burke, B. M. Gallant, J. Uddin, J. R. Greer, B. D. McCloskey, G. V. Chase, D. Addison, *J. Am. Chem. Soc.* **2016**, *138*, 2656.
[28] Z. Qi, H. Wang, *Research* **2020**, *2020*, 2969510.
[29] H. Yu, J. Xie, N. Shu, F. Pan, J. Ye, X. Wang, H. Yuan, Y. Zhu, *Research* **2019**, *2019*, 9129457.
[30] M. B. Jakubinek, C. O'Neill, C. Felix, R. B. Price, M. A. White, *Dent. Mater.* **2008**, *24*, 1468.
[31] L. Liu, C. Qiao, H. An, D. Pasini, *Sci. Rep.* **2019**, *9*, 19499.
[32] J. W. Boley, W. M. van Rees, C. Lissandrello, M. N. Horenstein, R. L. Truby, A. Kotikian, J. A. Lewis, L. Mahadevan, *Proc. Natl. Acad. Sci. USA* **2019**, *116*, 20856.
[33] T. van Manen, S. Janbaz, A. A. Zadpoor, *Mater Today* **2018**, *21*, 144.
[34] W. Xu, Z. Qin, C.-T. Chen, H. R. Kwag, Q. Ma, A. Sarkar, M. J. Buehler, D. H. Gracias, *Sci. Adv.* **2017**, *3*, e1701084.
[35] S. Yao, J. Cui, Z. Cui, Y. Zhu, *Nanoscale* **2017**, *9*, 3797.
[36] J. Cui, F. R. Poblete, Y. Zhu, *Adv. Funct. Mater.* **2018**, *28*, 1802768.
[37] Z. Liu, D. Qi, W. R. Leow, J. Yu, M. Xiloyannnis, L. Cappello, Y. Liu, B. Zhu, Y. Jiang, G. Chen, L. Masia, B. Liedberg, X. Chen, *Adv. Mater.* **2018**, *30*, 1707285.
[38] Z. Song, C. Lv, M. Liang, V. Sanphuang, K. Wu, B. Chen, Z. Zhao, J. Bai, X. Wang, J. L. Volakis, L. Wang, X. He, Y. Yao, S. Tongay, H. Jiang, *Small* **2016**, *12*, 5401.
[39] C. Yu, Z. Duan, P. Yuan, Y. Li, Y. Su, X. Zhang, Y. Pan, L. L. Dai, R. G. Nuzzo, Y. Huang, H. Jiang, J. A. Rogers, *Adv. Mater.* **2013**, *25*, 1541.
[40] X. Wang, Q. Liu, S. Wu, B. Xu, H. Xu, *Adv. Mater.* **2019**, *31*, 1807716.
[41] C. H. Lee, J.-W. Jeong, Y. Liu, Y. Zhang, Y. Shi, S.-K. Kang, J. Kim, J. S. Kim, N. Y. Lee, B. H. Kim, K.-I. Jang, L. Yin, M. K. Kim, A. Banks, U. Paik, Y. Huang, J. A. Rogers, *Adv. Funct. Mater.* **2015**, *25*, 1338.
[42] Z. Zhao, C. Yuan, M. Lei, L. Yang, Q. Zhang, H. Chen, H. J. Qi, D. Fang, *Phys. Rev. Appl.* **2019**, *11*, 044074.
[43] Q. He, S. Sun, L. Zhou, *Research* **2019**, *2019*, 1849272.
[44] Y. Jian, B. Wu, X. Le, Y. Liang, Y. Zhang, D. Zhang, L. Zhang, W. Lu, J. Zhang, T. Chen, *Research* **2019**, *2019*, 2384347.
[45] C. Zhang, H. Deng, Y. Xie, C. Zhang, J. W. Su, J. Lin, *Small* **2019**, *15*, 1904224.
[46] X. Cheng, Y. Zhang, *Adv. Mater.* **2019**, *31*, 1901895.
[47] Y. Ling, W. Pang, X. Li, S. Goswami, Z. Xu, D. Stroman, Y. Liu, Q. Fei, Y. Xu, G. Zhao, B. Sun, J. Xie, G. Huang, Y. Zhang, Z. Yan, *Adv. Mater.* **2020**, *32*, 1908475.
[48] H. Deng, X. Xu, C. Zhang, J. W. Su, G. Huang, J. Lin, *ACS Appl. Mater. Inter.* **2020**, *12*, 13378.
[49] Q. Luo, G. Garbarino, B. Sun, D. Fan, Y. Zhang, Z. Wang, Y. Sun, J. Jiao, X. Li, P. Li, N. Mattern, J. Eckert, J. Shen, *Nat. Commun.* **2015**, *6*, 5703.
[50] K. Takenaka, T. Shinoda, N. Inoue, Y. Okamoto, N. Katayama, Y. Sakai, T. Nishikubo, M. Azuma, *Appl. Phys. Express* **2017**, *10*, 115501.
[51] X. Jiang, M. S. Molokeev, P. Gong, Y. Yang, W. Wang, S. Wang, S. Wu, Y. Wang, R. Huang, L. Li, Y. Wu, X. Xing, Z. Lin, *Adv. Mater.* **2016**, *28*, 7936.
[52] C. W. Li, X. Tang, J. A. Munoz, J. B. Keith, S. J. Tracy, D. L. Abernathy, B. Fultz, *Phys. Rev. Lett.* **2011**, *107*, 195504.
[53] J. Chen, Q. Gao, A. Sanson, X. Jiang, Q. Huang, A. Carnera, C. G. Rodriguez, L. Olivi, L. Wang, L. Hu, K. Lin, Y. Ren, Z. Lin, C. Wang, L. Gu, J. Deng, J. P. Attfield, X. Xing, *Nat. Commun.* **2017**, *8*, 14441.
[54] K. Wei, H. Chen, Y. Pei, D. Fang, *J. Mech. Phys. Solids* **2016**, *86*, 173.
[55] N. M. A. Palumbo, C. W. Smith, W. Miller, K. E. Evans, *Acta Mater.* **2011**, *59*, 2392.
[56] H. Xu, A. Farag, D. Pasini, *Acta Mater.* **2017**, *134*, 155.
[57] L. Ai, X. L. Gao, *Compos. Struct.* **2017**, *162*, 70.
[58] H. Xu, A. Farag, D. Pasini, *J. Mech. Phys. Solids* **2018**, *117*, 54.
[59] H. Xu, A. Farag, R. Ma, D. Pasini, *J. Appl. Mech.* **2019**, *86*, 111011.
[60] E. Gdoutos, A. A. Shapiro, C. Daraio, *Exp. Mech.* **2013**, *53*, 1735.
[61] Y. Li, Y. Chen, T. Li, S. Cao, L. Wang, *Compos. Struct.* **2018**, *189*, 586.
[62] H. Zhu, T. Fan, Q. Peng, D. Zhang, *Adv. Mater.* **2018**, *30*, 1705048.
[63] C. A. Steeves, C. Mercer, E. Antinucci, M. Y. He, A. G. Evans, *Int. J. Mech. Mater. Des.* **2009**, *5*, 195.
[64] L. Ai, X. L. Gao, *Int. J. Mech. Sci.* **2018**, *135*, 101.

[65] J. Schwerdtfeger, F. Schury, M. Stingl, F. Wein, R. F. Singer, C. Körner, *Phys. Status Solidi B* **2012**, *249*, 1347.
[66] X. Li, L. Gao, W. Zhou, Y. Wang, Y. Lu, *Extreme Mech. Lett.* **2019**, *30*, 100498.
[67] O. Sigmund, S. Torquato, *Appl. Phys. Lett.* **1996**, *69*, 3203.
[68] O. Sigmund, S. Torquato, *J. Mech. Phys. Solids* **1997**, *45*, 1037.
[69] H. Heo, S. Li, H. Bao, J. Ju, *Adv. Eng. Mater.* **2019**, *21*, 1900225.
[70] S. Taniker, P. Celli, D. Pasini, D. C. Hofmann, C. Daraio, *Int. J. Solid Struct.* **2020**, *190*, 22.
[71] E. Boatti, N. Vasios, K. Bertoldi, *Adv. Mater* **2017**, *29*, 1700360.
[72] J. S. O. Evans, T. A. Mary, A. W. Sleight, *J. Solid State Chem.* **1998**, *137*, 148.
[73] J. S. O. Evans, T. A. Mary, T. Vogt, M. A. Subramanian, A. W. Sleight, *Chem. Mater.* **1996**, *8*, 2809.
[74] K. Takenaka, H. Takagib, *Appl. Phys. Lett.* **2005**, *87*, 261902.
[75] Y. K. Kwon, S. Berber, D. Tomanek, *Phys. Rev. Lett.* **2004**, *92*, 015901.
[76] H. Jiang, B. Liu, Y. Huang, K. C. Hwang, *J. Eng. Mater. Technol.* **2004**, *126*, 265.
[77] A. L. Goodwin, C. J. Kepert, *Phys. Rev. B: Condens. Matter Mater. Phys.* **2005**, *71*, 140301.